The influence of electron multiplication and internal X-ray fluorescence on the performance of a scintillator-based gamma camera

The influence of electron multiplication and internal X-ray fluorescence on the performance of a scintillator-based gamma camera

David J. Hall [a,*] Andrew Holland [a] Matthew Soman [a]

[a] *e2v centre for electronic imaging, The Open University, Walton Hall, Milton Keynes MK7 6AA, UK*

Abstract

When considering the 'standard' gamma-camera, one might picture an array of photo-multiplier tubes or a similar array of small-area detectors. This array of imaging detectors would be attached to a corresponding array of scintillator modules (or a solid layer of scintillator) in order to give a high detection efficiency in the energy region of interest, usually 8-140 keV. Over recent years, developments of gamma-cameras capable of achieving much higher spatial resolutions have led to a new range of systems based on Charge-Coupled Devices with some form of signal multiplication between the scintillator and the CCD in order for one to distinguish the light output from the scintillator above the CCD noise. The use of an Electron-Multiplying Charge-Coupled Device (EM-CCD) incorporates the gain process within the CCD through a form of 'impact ionisation', however, the gain process introduces an 'excess noise factor' due to the probabilistic nature of impact ionisation and this additional noise consequently has an impact on the spatial and spectral resolution of the detector. Internal fluorescence in the scintillator, producing K-shell X-ray fluorescence photons that can be detected alongside the incident gamma-rays, also has a major impact on the imaging capabilities of gamma-cameras. This impact varies dramatically from the low spatial resolution to high spatial resolution camera system. Through a process of simulation and experimental testing focussed on the high spatial resolution (EM-CCD based) variant, the factors affecting the performance of gamma-camera systems are discussed and the results lead to important conclusions to be considered for the development of future systems. This paper presents a study into the influence of the EM-CCD gain process and the internal X-ray fluorescence in the scintillator on the performance of scintillator-based gamma cameras (CCD-based or otherwise), making use of Monte Carlo simulations to demonstrate the aspects involved, their influence on the imaging system and the hypotheses previously discussed in experimental studies.

Key words: Gamma camera, CCD, EM-CCD, scintillator, resolution, fluorescence

1 Introduction

There are many applications for gamma-cameras in the energy regime from 8-140 keV, from medical imaging to synchrotron-based research. It is generally possible to split current gamma-camera technology into two groups: low spatial resolution and high spatial resolution systems. Here, low-resolution gamma-cameras are defined as those with a resolution of a few hundred micrometers or greater. High-resolution gamma-cameras are defined here as those with a resolution of better than 100 µm. The grouping occurs in this way due to the technologies behind the detectors available for such camera systems. Gamma-cameras can be made from arrays of imaging detectors, each detector creating a 'single pixel' and generally measuring a few hundred micrometers across. Such camera systems generally have lower resolutions in the spatial regime but comparatively better spectral resolutions [1]. Alternatively, one can manufacture a high-resolution gamma-camera from a single imaging device for which each pixel is a few tens of micrometers in size [2]. Although such detector systems can have much higher spatial resolutions, the spectral resolution generally suffers (Sections 3 and 4).

In order to create the highest-resolution gamma-cameras, sub-pixel imaging is required and can be achieved through photon-counting imaging techniques and centroiding. The low numbers of photons recorded per event when using photon-counting techniques can be lost beneath the readout noise floor of a standard Charge-Coupled Device (CCD). If one uses an Electron-Multiplying Charge-Coupled Device (EM-CCD), then the effective readout noise can be reduced to the sub-electron level, dramatically increasing the effective signal-to-noise level. However, the gain process ('impact ionisation') required to increase the effective signal-to-noise ratio introduces an additional noise factor, the so called 'gain noise'. This additional noise factor acts to reduce the spectral resolution and can be studied analytically, but the effect of the additional noise on the centroiding accuracy is more complex and hence a simulation has been produced to ascertain the level of impact of the gain process on the ability to achieve sub-pixel imaging in comparison to a similar CCD system to allow a spatial imaging performance comparison to be made.

When using a silicon-based detector for gamma-ray imaging, it is generally preferential to increase the detection efficiency through the use of a scintillator, either directly coupled to the detector or through a fibre-optic system. With a scintillator based detection system, experimental results suggest the K-shell fluorescence X-rays that can be generated in the scintillator from the incident gamma-rays (provided they are of energy greater than the K-shell binding

* Corresponding author.
Email address: d.j.hall@open.ac.uk (David J. Hall).

energy) can be reabsorbed at another location in the scintillator, acting to decrease the spatial resolution of the system. Although thresholding can be used to a certain extent, this brings a dramatic reduction in the detection efficiency as, for the example of the scintillator CsI(Tl), approximately 90% of 'true' events can be rejected. Using a series of new simulations, validated against previously reported experimental results [2–5], to look at both the spatial and spectral capabilities of the detector systems, the impact on the resolutions of the internal fluorescence is explored for both 'high' and 'low' resolution gamma cameras.

This work develops on theory and experimental results taken from [2–5] and the PhD thesis by the author [6], with the theory in Sections 2 and 5 taken from this work. Through new additional simulations and analysis this study aims to confirm the hypotheses presented in the previous experimental work and to place the results in a wider context, developing the scope to include limitations on the camera system. For every application of the gamma-camera the desired specifications may change. Through consideration of the systems as a whole, taking into account, for example, the limitations on the spatial resolution due to the use of a collimator, the choice of system can be considered. The first choice to be made is between that of a spatially or spectrally preferential system. The choice of one detector over another is discussed and possible improvements to the detector systems inferred.

2 The scintillation process

Scintillators have been dominant in the field of ionising radiation detection for over one hundred years. Solid scintillation was first observed by Elster and Geitel in 1903, where the presence of an alpha-emitting source led to individual light flashes in a ZnS screen [7]. Over the last century, developments in the understanding of the scintillation process and the discovery of new scintillating materials has led to many new uses throughout high-energy physics and astrophysics, along with the continual development for medical imaging applications from the first X-ray film through to modern dental CCD imagers.

A scintillator converts the energy from the absorption of ionising radiation into a flash of photons of a much longer wavelength, usually in the visible region of the electromagnetic spectrum. In the case of the gamma-ray detection, the combination of the larger number of output photons compared to the incident flux and the lower energy of the photons produced means that scintillators are a near ideal choice for coupling to a silicon based imager (such as a CCD or CMOS device). As most higher energy X-rays will pass straight through the silicon of the device (with no scintillator present) the detection efficiency for high energy photons is much reduced. Through the inclusion of a thicker

scintillating layer, the detection efficiency can be greatly increased.

2.1 Inorganic scintillators

The scintillator acts to convert a single high-energy quantum into many lower energy quanta. The reduction in energy of the quanta to be detected leads to a much higher efficiency of detection than would be possible with the higher energy quantum.

The scintillation process can be described in five stages as detailed in [8]:

(1) Creation of electron-hole pairs through the absorption of ionising radiation.
(2) Relaxation of primary e-h pairs, producing multiple secondary electrons, holes, photons, phonons and other electronic excitations.
(3) Thermalisation of secondary e-h pairs through interactions with the vibrations of the environment.
(4) Energy transfer to the luminescence centres.
(5) Emission of energy from luminescence centres in the form of lower energy photons.

At the energies considered in this study, the photo-electric effect dominates due to a larger interaction cross-section than the Compton interactions, Figure 1. Through the photoelectric effect, a hole is created in the inner electron shell of the atom (K-shell). This leaves an ionised atom and a free electron with energy equal to $h\nu$ minus the binding energy of the electron. The ionised atom in the lattice may relax through the emission of a photon, as another electron drops to fill the hole, or through the Auger effect, where further electrons are released. The electrons then lose energy through further scattering or the emission of photons. This process continues until ionisation is no longer possible. Electrons lose excess energy through inelastic scattering until only low energy excitations in the lattice remain.

When the energy of the excited electrons is below the ionisation threshold, the electrons begin to interact with vibrations in the environment: the process of thermalisation. The holes move to the top of the valence band, whilst the electrons move to the bottom of the conduction band, leaving many electron-hole pairs each separated by the band gap energy E_g. This stage leaves N_{eh} electron-hole pairs, Equation 1, where ε is the average energy required to create a single electron-hole pair and E_γ is the energy of the incident absorbed photon [8].

$$N_{eh} = \frac{E_\gamma}{\varepsilon} \tag{1}$$

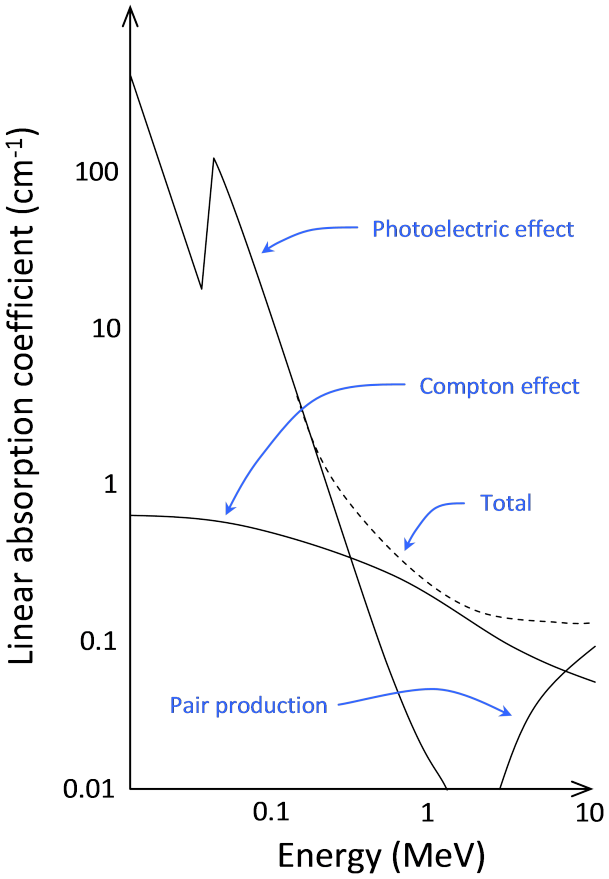

Fig. 1. The linear absorption coefficient for CsI(Tl) against incident gamma-ray energy. The photo-electric effect dominates in the region of interest in this study (below 200 keV).

The electronic excitations then transfer their energy to the luminescence centres in the scintillator (such as the Tl^+ ions in CsI(Tl) that are involved in the electronic recombination). The luminescence centres can be excited through either the consecutive capture of an electron then a hole (hole recombination luminescence) or a hole then an electron (electron recombination luminescence) [8]. The emission of photons follows the relaxation of the excited luminescence centres to their ground state.

2.2 Thallium-doped caesium iodide

Thallium doped Caesium Iodide is a popular scintillator choice for current gamma-cameras due to the high emission yield (54 photons per keV gamma), the similar refractive index to that of glass in a fibre-optic plate (1.79 at emission maximum) and the low self-absorbance (re-absorbance of emitted photons) for the slow component (3.4±0.5 µs), despite the higher self-absorbance of the fast component (600±50 ns), although this will depend on the crystal

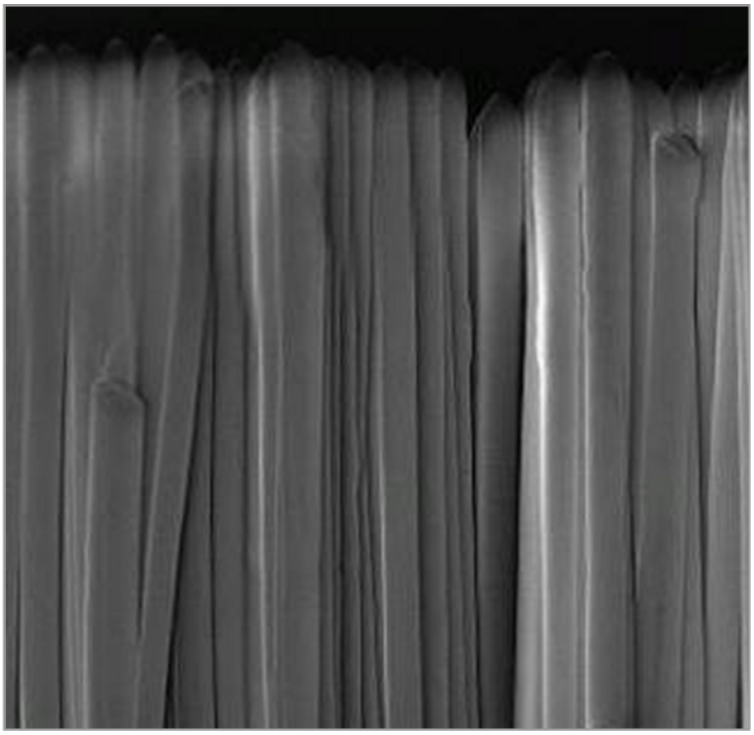

Fig. 2. An SEM of the scintillator CsI(Tl). The scintillator can be seen to be formed of columns of diameter 5-6 µm. The sample used in this study was produced by e2v technologies with a thickness of 70 µm [11].

dimensions [9,10]. The scintillator can also be grown in a columnar form that, although not perfect, reduces the spread in the light emitted in the scintillator, Figure 2. In a similar way to a fibre-optic plate, the scintillator acts to channel the light to the CCD along the columnar structures, acting to reduce the light spread and increase the peak in intensity of the Gaussian-like profile observed at the CCD surface.

The scintillator produces approximately 60 photons per keV of incident energy, forming an approximately linear dependence on energy over the range of interest. Through the analysis of the number of photons emitted, it is in theory possible to relate this figure to the energy of the incident photons [4,8].

2.3 Internal X-ray fluorescence

Interactions occurring in the scintillator due to gamma-ray irradiation must be studied in greater detail in order to ascertain the imaging capabilities of a scintillator-based camera system. The interaction process inside the scintillator does not simply supply a series of identical scintillation flashes all occurring at the incident gamma-ray energy. At low energies (below the binding energies of elements in the scintillator) the interaction process is simplified and

the number of lower energy photons produced is proportional to the incident photon energy, with one reaction point for each incident quantum.

For caesium iodide, the scintillator used as a demonstrator in this study, the binding energies of importance are those for caesium at 35.99 keV and iodine at 33.17 keV. Incident photons of energies below approximately 30-35 keV are not of interest here as these will provide a single spectral peak. For the imaging of harder X-rays, those above approximately 30-35 keV, one has to consider the impact of K-shell fluorescence on the imaging capabilities of the system.

Considering the case of a ^{241}Am source providing incident gamma-rays at 59.5 keV, one can discuss the internal X-ray fluorescence further. Approximately 90% of interactions in the caesium iodide at 59.5 keV will be due to the photo-electric effect. Of these primary interactions, the fluorescence yield is approximately 88-90%, resulting from electrons falling from higher energy levels to fill the hole left by the ejected electron [12]. In this case, the difference between the interaction probability with the caesium and iodine atoms is negligible.

At 59.5 keV, the incident photons have sufficient energy to knock an electron from the inner shell of the caesium and iodine atoms in the scintillator, releasing an electron of energy equal to the incident photon energy (59.5 keV in this case) minus the binding energy of the atom (either caesium or iodine in this case). The ejected electron has insufficient energy to travel far from the initial interaction point, but may traverse several microns. Remaining excitations in the atom, along with the scintillation caused by the ejected electron, provides the flash of photons at (or very close to) the initial interaction position.

Following this process, approximately 10% of the relaxations of the atoms follow the Auger process. The ejected electrons will cause scintillation surrounding the initial interaction position and the total sum of the number of lower energy photons produced at this point will be proportional to the incident photon energy.

The remaining 90% of relaxations result in K-shell X-ray fluorescence, where an outer shell electron falls to fill the hole left by the ejected electron, releasing the difference in energy in the form of a characteristic X-ray. Kα emission results from approximately 90% of these interactions, with the remaining 10% resulting from Kβ emission. The emitted characteristic fluorescence X-rays may travel through the scintillator and leave the material undetected. In this case, the number of lower energy photons produced relates to the energy of the emitted electron. If, however, the fluorescence X-ray interacts with the scintillator, a secondary interaction site will occur away from the initial interaction point, with the distance between the two interaction sites determined by the

probability of interaction at the energy of the fluorescence X-ray. It is this distance between the initial interaction and the secondary event that affects the imaging capabilities of the device. This process was observed in [13,14] as a "separately resolved primary interaction and the secondary K X-ray interaction", giving an 'extra' event outside the line of a slit placed over the camera. Here we aim to determine the impact of the detection of these 'extra' events on the spatial and spectral resolution using simulations designed to confirm and explore the results detailed in the experimental studies and the affect the re-absorbed fluorescence on 'high' and 'low' spatial resolution gamma cameras [2,13,14].

3 Gamma cameras based on photo-multiplier tubes

Until recently, a standard gamma-camera consisted of an array of Photo-Multiplier Tubes (PMTs) coupled to a thick scintillating layer [1]. When an X-ray photon interacts in the scintillator a flash of photons is produced that can be detected as a series of voltages from the PMT array . The coincidence of signals from a sub-array of PMTs close to the interaction location allow a weighted mean position to be calculated from the relative signals between the PMTs in the sub-array. The total sum of the signal from all detectors in the PMT array is proportional to the energy deposited in the interaction of the incident photon. In the past, PMT arrays have been limited to providing intrinsic detector spatial resolutions of the order of 3-5 mm depending on the crystal type and thickness, PMT dimensions and algorithms used [1]. However, current systems are capable of sub-millimetre precision down to a suggested limit of 0.5 mm [15], although it is noted that the spatial and energy resolution depend strongly on the scintillator used and the corresponding light output, limiting the FWHM energy resolution to approximately 9-11% for NaI(Tl) [1,15].

Performance in such detectors varies, dependent on the scintillator used and detector arrangements. Energy resolutions of 22-24% have been reported for CsI(Tl), in comparison to an improved performance of 14% for NaI(Tl) for the same detector formulation [16], with a best case energy resolution of 10.8% FWHM achieved with NaI(Tl) [17]. Spatial resolutions were also recorded at 0.6-0.9 mm and 1.16 mm respectively, reaching the sub-millimetre level, but still a long way from the sub-100 µm levels achievable with high resolution camera systems (Section 4). Another example is that described in [18], in which a 3 mm NaI(Tl) crystal was coupled to a PMT array ("Hamamatsu H5900-00-C12, 1-inch square cross-wire readout type") to create a small FOV gamma-camera. The spatial resolution in this case was limited to 1.5 mm, although more recent developments of this system have led to an improvement in spatial resolution to 0.75 mm at 122 keV using a 2 mm thick $LaBr_3$(Ce)

scintillator [19]. The use of a scintillator with improved light output has in this case also brought improvements in the energy resolution to 8.9% and 13.4% at 122 keV and 60 keV respectively. Similar results of 0.9 mm FWHM spatial resolution have been reported in [20] using a $LaBr_3$(Ce) scintillator and position sensitive PMT.

4 CCD-based gamma cameras

Following from the description above of a 'low spatial resolution' gamma-camera, one can consider what is required to image at a much higher spatial resolution. One of the main limiting factors of the aforementioned systems is the use of an array of PMTs. The limit on the physical size of each 'pixel' in the PMT array provides an optimal resolution limit above which such a system could not deliver. One way of improving the spatial resolution of a 'standard' gamma-camera is to replace the PMT array with an 'array of detectors' for which the individual element size is much reduced - a CCD or CMOS/hybrid based system.

In order to cope with applications in which a high-flux rate is required, the readout speed of the detector must be increased to enable the use of 'photon-counting' techniques (Section 8.1). Unfortunately, an increase in the readout speed of a CCD leads to an increase in the readout noise. This increase in readout noise would not allow the detector to distinguish low signal levels above the random fluctuations in the 'zero-level' of the image. Without any readout noise and no signal present (of any type) then one would expect a flat field image of zeros (a true 'zero-level'). However, with read noise, this flat field of zeros is altered such that the 'zero-level' fluctuates due to the random noise measured at the output of the camera system [21]. The increase in readout noise can, however, be counteracted through the use of off-chip or on-chip amplification of the signal - increasing the signal level before the addition of the readout noise component.

The early development of the 'BazookaSPECT' system demonstrates the use of off-chip signal amplification through the use of a second generation imaging intensifier and lens system to amplify the signal from the scintillator before reaching the CCD [22,23]. In comparison with the systems described previously, very high spatial resolutions can be achieved down to 50 µm. As the name of the system suggests, however, there are physical detector system dimension limitations that may only be overcome through the use of on-chip signal amplification.

5 On-chip signal amplification

The number of signal electrons in a charge packet in a CCD can be increased through the process of 'impact ionisation' [21]. When a controllable high voltage is placed over a CCD electrode, creating a high electric field between this and neighbouring electrodes, the 'impact ionisation' process can be controlled. With an increase in the signal charge and no subsequent increase in readout noise, the 'effective readout noise' (compared to original signal level) can be reduced to the sub-electron level.

5.1 The Electron-Multiplying CCD

The Low-Light-Level camera uses an Electron-Multiplying CCD (EM-CCD) [24] to provide all light level imaging from bright sunlight down to shadowed overcast starlight. The variable gain allows the device to be run as a standard CCD in sunlight with unity gain and also down to very low light levels by increasing the gain level. The multiplication of the signal before readout effectively reduces the readout noise which can be reduced to the sub-electron level [25]. The very low readout noise allows the detection of signals of only a few photons, signal levels which would otherwise be lost beneath the readout noise of a standard CCD.

EM-CCDs have many uses, from 24-hour surveillance to military imaging at night. The flexibility of the camera has led to the technology being exploited in night-time surveillance [26], scientific imaging [27] and medical imaging [28]. The EM-CCD shares the same basic structure as a standard frame-transfer CCD. The main difference between the EM-CCD and a standard frame-transfer CCD is the addition of a gain register following on from the standard readout register.

5.2 The gain process

When an electron passes through a region of high-electric field it can be accelerated. If an electron passes through a region of high electric-field in silicon then the electron can gain sufficient kinetic energy to effectively slam into the lattice, breaking the silicon-silicon covalent bonds, the process of 'impact ionisation' [21]. The generated electrons can in turn gain enough kinetic energy to break further bonds, creating extra electron-hole pairs and causing further impact ionisation.

Although this process can generate spurious signal through the formation of

electron-hole pairs from non-signal electrons, the process can be controlled through the application of specific voltages to a specially designed gain structure in the CCD where the probability of impact ionisation increases as the electric-field increases in magnitude. Varying the voltage applied to the multiplication electrode structure alters the electric-field and allows the gain process to be controlled.

Due to the stochastic nature of the multiplication gain, during the gain process each signal electron can be assumed to behave independently and may generate a different number of avalanche electrons. The excess noise factor, F, a measure of the ratio of the noise on the signal at the input to the gain register compared to that at the output (for optical photons) where G is the total multiplication gain, $\sigma^2_{n_{in}}$ is the variance on the signal before the gain process and $\sigma^2_{n_{out}}$ is the variance of the output signal, is defined as [29]:

$$F^2 = \frac{\sigma^2_{n_{out}}}{G^2 \sigma^2_{n_{in}}} \tag{2}$$

For a large number of transfers across the gain register (as found in the EM-CCDs produced by e2v technologies), this formula can be solved [6] to produce:

$$F^2 = \frac{2G - 1}{G} \tag{3}$$

To a first approximation, F tends to $\sqrt{2}$ for high gain factors (tens to hundreds) [29]. For optical photons the variance on the signal levels measured, assuming Poisson statistics are valid, is equal to the mean signal level, therefore although gain process allows low-signal levels to be increased above the readout noise, the noise on the signal level itself increases [29]. For very low signal levels where high levels of gain are required, the gain process effectively doubles the variance on the signal level. The impact of this increase in noise will be considered further in Section 8.2. It is worth noting that this is only the case for optical photons. If direct detection of X-rays was to be used, where the Fano factor must come into consideration, the noise on the gain process becomes more complicated [30].

6 EM-CCD based gamma-cameras

The use of off-chip signal amplification can be replaced by the use of an Electron-Multiplying CCD (Section 5.1), such as in the early development of the Ultra Gamma Camera (UGC) [31]. In this case, a 1 mm thick CsI(Tl) layer was coupled to an EM-CCD through the use of a fibre-optic taper. The

EM-CCD used contained rectangular pixels (20 × 30 µm), resulting in different spatial resolutions in the two dimensions of 60 µm and 100 µm at 122 keV. Using the peak signal in each event detected, 'energy peaks' can be observed at 122 keV and 28 keV using two different sources, although the broadening of the spectrum to lower energies causes an overlap with the 28 keV peak such that one cannot determine the origin of photons measured at lower energies (if both sources were present).

Each X-ray interacting in the scintillator will do so at a different depth and will therefore generate a signal at the EM-CCD with a differing 'spread': the so called 'depth of interaction' (DOI) effect. Early attempts at producing an energy spectrum from interacting events detailed in [31] use the peak signal in an event as a measure of the energy of the X-ray interacting. Whilst this gives 'energy peaks', the DOI effects broaden the spectrum such that the broad peaks overlap on a large scale.

Developments in energy detection techniques in an attempt to remove scattered events produce improvements in the spectrum, but energy resolutions of 40 keV and 42 keV at 122 keV and 28 keV respectively [32] show that the technique is limited in comparison to the previously discussed detectors. A higher detector resolution combined with energy discrimination capabilities has been said to be essential for future Single Photon Emission Computed Tomography (SPECT) systems [33], but measurements of the energy resolution of 33 keV at 140 keV left a requirement for further study, despite the improvements in the spatial resolution. More recently, a spatial resolution of 59.4 µm was reported using a CCD97 [34].

The method used to extract the energy spectrum from the raw X-ray interaction events in the scintillator recorded in the EM-CCD has a major impact on the energy resolution achieved. Developments to incorporate binning of the signal in each event begin to take into account the DOI effects that are ignored in simple 'peak signal' techniques. However, DOI effects can be approached from two further directions. A Maximum Likelihood Estimation (MLE) technique was used in [14], incorporating a calibration stage in the device development, aiming to use recorded events of known DOI to determine the DOI of events recorded when imaging. The second approach makes use of 'scale-space', a form of Wavelet transform, developed from algorithms used in computer vision [35], adapted to improve the resolution of gamma-cameras [3]. Applications of these techniques to improve the resolution of cameras showed great promise when applied to simulated data [3] and have been further developed with respect to experimental data [4] using the camera described below. The same technique has also since been detailed in [36] in which it was found to offer significant improvements over the techniques described above (as in [32]), although still limiting the energy resolution a best-case of over 40% energy resolution at 140 keV and a spatial resolution of 59 µm.

7 Event separation

The results shown in Figure 3 are taken from a Monte Carlo simulation designed to investigate the influence of the re-absorbed fluorescence on the spatial resolution of the detector. A 'block' of scintillator, CsI(Tl) has been simulated with dimensions of 1 cm $\times$ 1 cm $\times$ t µm, where t is the scintillator thickness (here shown at 70 µm, 350 µm and 700 µm). A set flux of incident photons is entered into the system along the normal to the imaging plane using a random distribution in the xy plane. Each incident photon to the simulation is generated with a randomly generated interaction distance (based on the interaction length) that will either fall within or outside of the block of scintillator. Photons that do not interact within the scintillator are lost from the system. Photons that interact within the scintillator, using standard Monte Carlo techniques, will generate a fluorescence X-ray as appropriate based on the probabilities discussed in Section 2. If a fluorescence X-ray is emitted, then this photon will travel in a randomly generated direction away from the production position and this is then tracked until interaction or exit from the scintillator structure (as with the primary photons). All locations of interactions are recorded and the distance travelled in the xy-plane (the plane of the detector pixels) is then calculated and this is shown in the distributions in Figure 3. The incident photons are able to interact at any position in the scintillator as determined by probability of interaction defined by the interaction length and the scintillator dimensions. This 'realistic' positioning of the initial interaction positions ensures the emitted fluorescence photons will pass through the scintillator having been generated across the scintillator with no bias. If one considers the distance between the primary and secondary interaction positions from the simulated results shown in Figure 3, it is clear that negligible signal will be detected outside a millimetre in radius from the primary interaction location.

With a spatial resolution of the order of 0.5 millimetres and above, one is forced to consider the majority of primary and secondary events as 'single' events. In this way, the sum of the energy deposited in the primary and secondary interactions is recorded for this 'single' event, albeit with a bias on the positioning of the interaction position from this combination of the original interaction and the re-absorbed fluorescence X-ray, further degrading the spatial resolution.

Despite the apparent limits on the spatial resolution, the grouping of the energy deposited from primary and secondary interactions leads to a high spectral resolution (as high a resolution as 6% FWHM at 140 keV and 3% FWHM at 662 keV [37]). The presence of the secondary interactions has a major impact on not only the ability to achieve a higher spatial resolution, but also a major impact on the spectral resolution of the detector.

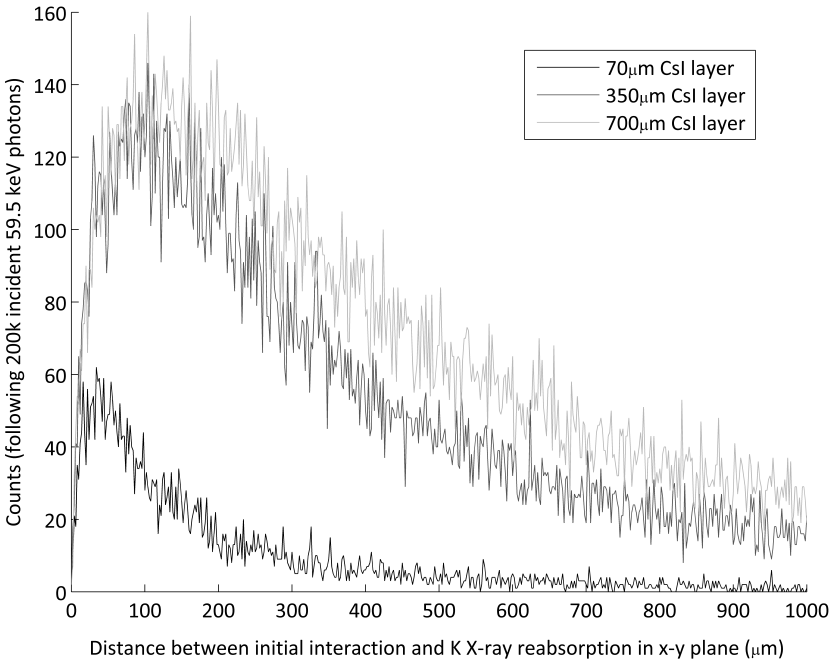

Fig. 3. The interaction distance for the fluorescence X-ray produced in CsI, simulated here for scintillator thicknesses of 70 µm, 350 µm and 700 µm with a constant incident flux. The results are presented in the xy plane only, as this is the plane in which an image would be taken. As the distance approaches 1 mm, it is seen that the number of counts has rapidly decreased.

8 Scintillator-coupled EM-CCD

In order to demonstrate the spatial and spectral capabilities of a gamma camera designed for high spatial resolution applications, a 70 µm columnar CsI(Tl) scintillator layer has been coupled to an e2v CCD97 [38] through a fibre-optic plate (approximately 3 mm thick). The CCD97 has been operated here with a pixel readout rate of 1 MHz for demonstration purposes but can be operated at up to 15 MHz with appropriate drive electronics. The increased amplifier noise introduced through increasing the readout rate has a negligible impact on the image output from an EM-CCD detector as the multiplication gain can simply be increased to reduce the effective readout noise to the sub-electron level [25].

8.1 Photon-counting

The standard operation of a CCD-scintillator imaging system, such as those used in dental imaging, involves the integration of signal over a pre-defined period of time. During this time period, any light generated in the scintillator

that is collected by the CCD will be summed to create a single contrast image. Any spread of light in the scintillator away from the initial interaction location will be summed in the image, degrading the spatial resolution by adding a secondary (wider) Gaussian profile in the Edge Spread Function (ESF), thus causing the rapid drop in MTF at low spatial frequencies, Figure 4(a).

An alternative method of operation involves the capture of many images over much shorter integration times such that each image contains a number of individual interactions, with each interaction separated by several pixels from the next. Through the analysis of a batch of images of this type, one can improve the imaging capabilities of the camera system dramatically. This 'photon-counting' technique is not straightforward and there are many factors that must be overcome, such as the impact of the depth of the primary interaction in the scintillator on the spread of the event observed by the detector [3]. Once these challenges have been considered, the batch of images can be analysed using a variety of methods on an event by event basis (Section 6).

A simple tungsten edge was placed against the scintillating layer to act as a mask to the incident X-ray photons, in this case emitted from a solid ^{241}Am source (59.5 keV) with an activity of 18.4 kBq at the time of the experiment. The 0.5 mm thick tungsten edge prevents approximately 95% [39] of the incident 59.5 keV photons from reaching the scintillator. The transmitted photons produce a small reduction in contrast between the covered and uncovered areas of the CCD97. The active area of the ^{241}Am source is in the form of a disc of diameter 5 mm. A thin layer of silver foil is present in the source holder, contributing a small amount of Kα X-ray fluorescence with an energy of 22 keV to the lower energy peaks in the spectrum. With the source placed at a distance of 4 cm from the tungsten edge, the geometry of the system broadens the spatial resolution that is measured, giving a spreading of the incident photons 'under the tungsten edge' across a width of approximately 6$\pm$2 microns (depending on the exact alignment) on the back surface of the scintillator due to the angular incidence of the X-rays. Further improvements in the measured spatial resolution would be expected if a columnar beam of incident photons was supplied to the system, but the arrangement used here allows a proof of concept study to be undertaken in which the results can be compared with that of the 'low resolution gamma cameras' discussed earlier. K series tungsten fluorescence is of too high an energy to be generated from the 59.5 keV incident photons (the K absorption edge for Tungsten has an energy over 59.5 keV) and the L series fluorescence (12.6 keV and below) will be removed during thresholding of the images if present.

Following the extraction of the individual events from the images using a technique described in [4] where it is possible to adjust the event selection criteria to fit the detector environment and application, it is possible to centroid the events such that a new 'integrated' image can be created from the individual

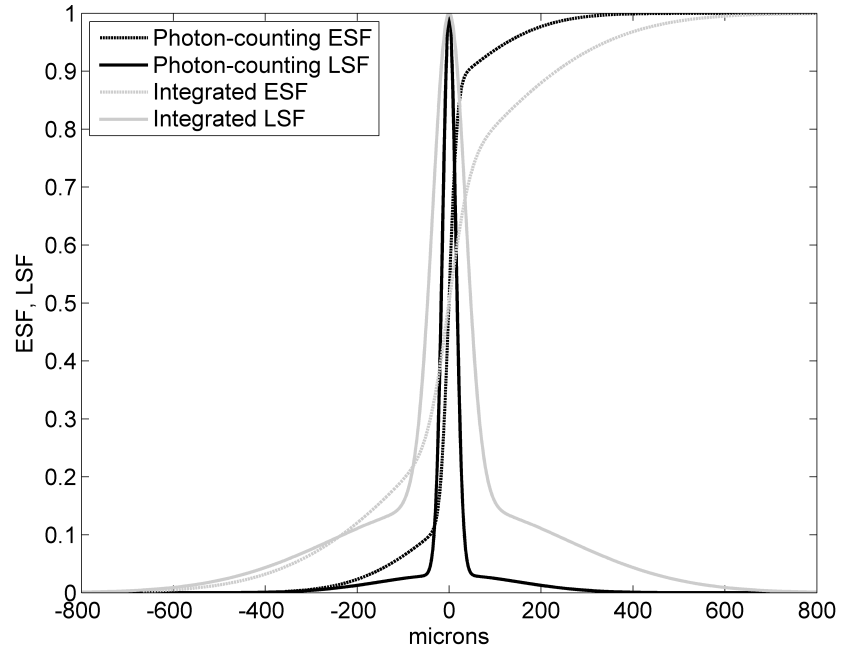

(a) Line Spread Function (LSF) and Edge Spread Function (ESF).

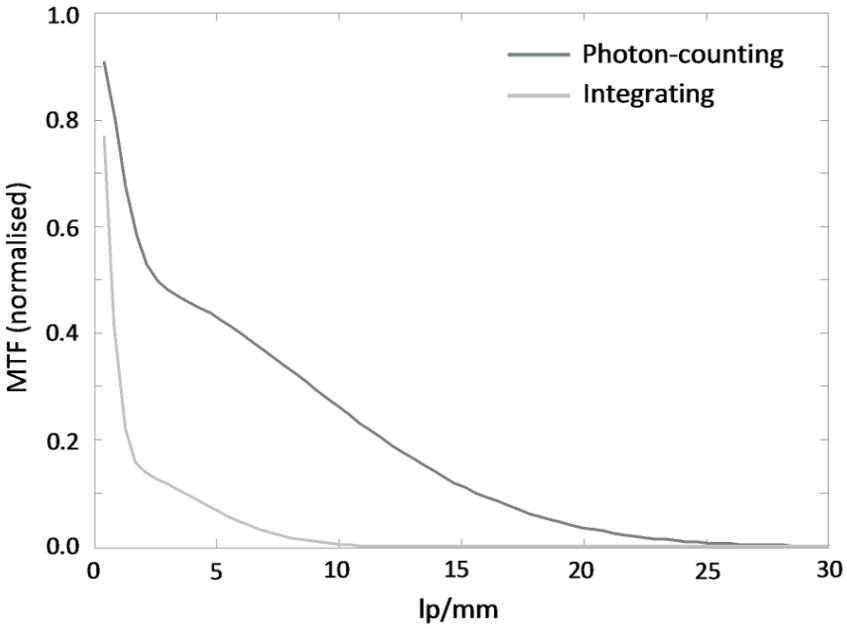

(b) Modulation Transfer Function (MTF).

Fig. 4. Fits taken to experimental data at 60 keV in integrating and photon-counting modes. (a) The LSF is not formed from a single Gaussian profile but is instead formed from the sum of two independently characterised profiles. (b) The resulting MTF, taken as the discrete Fourier transform of the LSF, showing the 'knee' in the curve due to the two components of the LSF. [2]

centroid locations. Through the use of this process, one can remove the effect of the spread in the light generated in the scintillator.

8.2 Spatial resolution

Experimental results presented in [2] detail the spatial capabilities of such a detector, as summarised in Table 1 and Figure 4. It must be noted that the line spread function (LSF) is not formed from the standard Gaussian-like profile. The complication in the ESF and LSF profile introduced was proposed to be due to the addition of a secondary Gaussian component to the LSF (such that profile can be fitted with the sum of two Gaussian profiles, both centred at the same position) due to re-absorption of the internal fluorescence X-rays [2]. A narrow profile represents the standard detector LSF with a broader component found at a lower count rate.

Imaging method	FWHM of LSF
Integration (standard)	80 µm
Photon-counting	31 µm

Table 1
Spatial resolution measurements for the scintillator-coupled EM-CCD in integrating and photon-counting modes [2].

8.3 Spectral resolution

With the approximately linear relationship between the light output of the scintillator and the incident photon energy, several methods are available to produce an energy spectrum of events. The use of the photon-counting mode is essential for this purpose; in the integrating mode all energy information is lost. The most simple method involves the use of the peak intensity of each event [31]. This does not, however, make allowances for the variation in the event profiles with depth of interaction in the scintillator, hence producing sub-standard results. This method can be improved through the summation of the central pixel of the events with surrounding pixels, now including the edges of the Gaussian profiles [2]. Unfortunately, for every extra pixel included in this summation, additional noise is also included. Using more complex methods, such as the use of Scale-Selection as discussed in [3,5,36], one is able to produce more detailed information about each event, such as the inference of the depth of interaction in the scintillator from the spread of the photons in the event profile.

With the requirements on detectors to enable high-resolution imaging, the detector noise is a limiting factor unless an EM-CCD is used to reduce the ef-

fective readout noise to the sub-electron level. In reducing the effective readout noise, one must use a gain process to increase the number of signal electrons. This gain process introduces an approximate increase in the noise level on the signal of $\sqrt{2}$ (as discussed in Section 5.2). Taking an ^{241}Am event in 70 µm of CsI(Tl), as implemented in [2], a peak signal (in the central pixel of an event hitting the centre of a pixel) of approximately 40 photons was measured when considering the 30 keV components that dominate the spectrum. If a more efficient coupling mechanism is used between the scintillator and detector then it is possible to increase the number of photons detected, whilst if a less efficient coupling mechanism is used then fewer photons may be recorded. If a fibre-optic taper is used, one must include the associated losses involved. The directly neighbouring pixels were found to have 5-25 photons each (dependent on photon hit position in the pixel) in the previous study [2]. Using simulated Gaussian profiles one is able to determine a 'best-case' energy resolution from an approximation to the light spread, multiplication noise components and intrinsic scintillator resolution. The results presented in Figure 5 are based on the experimental results with respect to the form of the event profiles achieved with the CsI(Tl) detector system detailed in this paper and literature values are used for the comparisons to NaI(Tl) and $LaBr_3$ and for the incorporation of the fibre-optic tapers [8,40]. These predicted results compare well with the experimental system detailed in Section 8, taking measurements from the experimental spectra shown in Figure 7, and demonstrate that there are indeed limitations on the energy resolution achievable with such systems formed from scintillator-coupled EM-CCDs. In comparison to the specific experimental detector system detailed in this study and the spectra recorded for Am^{241} and Co^{57}, it can be seen in Figure 5 that the performance is verging on the intrinsic performance limits achievable with such coupling.

9 Simulating a scintillator-based gamma-camera

In order to facilitate a better understanding of the camera system, several new simulations have been produced, allowing the demonstration and explanation of the effects noted in previous experimental studies and investigation of their impact. The energy deposition and localisation in the scintillator has been simulated, making use of the interaction lengths of each photon energy in the scintillator (CsI in this case). Using a three dimensional scintillation body, random directional generation for each X-ray photon following interaction in the scintillator allows the position of the event profile in the plane of the EM-CCD to be modelled. The interaction chain for the simulation is based on Figure 6, detailing the emission and re-absorption (or loss) of fluorescence photons. From the experimental results of [2] it was suggested that the 'two Gaussian' profile of the LSF was caused by the re-absorbed fluorescence com-

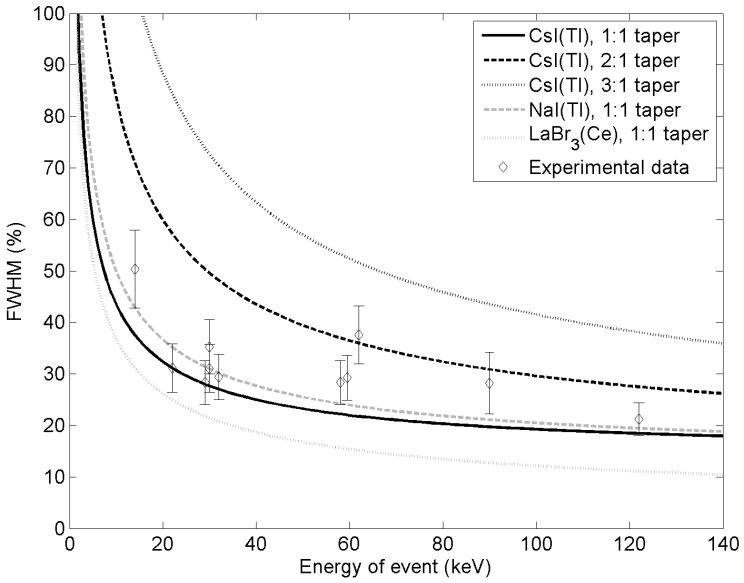

Fig. 5. Expected best-case energy resolution for the experimental camera system (CsI:Tl with a 1:1 fibre-optic taper) over a range of energies. Literature values for different scintillators [8] have been incorporated to predict the performance of similar systems following a change in scintillator or fibre-optic taper. The experimental results taken from Figure 7 for Am^{241} and Co^{57} are shown for comparison with the theoretical calculations and demonstrate that the detector detailed in this study is verging on the intrinsic limits for the coupling system used.

ponent, resulting in the curvature at the edges of the ESF (Figure 4(a)). These simulations aim to demonstrate the effect of the imaging of the fluorescence X-rays through a test-case simulation of the "perfect detector'. The "perfect detector" is assumed to have an MTF of one across all spatial frequencies and a scintillator in which the visible photons generated in the scintillator do not spread out as they pass towards the EMCCD. Therefore any degradation in resolution (or degradation of the ESF from a simple step function) is caused by the detection of the X-ray fluorescence. Also of interest here is the impact of the interaction chain (as detailed in Figure 6) on the spectral performance.

9.1 Spectral performance

Two spectra, measured using the experimental set-up detailed in Section 8.1 using a CCD97 and CsI(Tl) scintillator, for Am^{241} (18.4 kBq) and Co^{57} (70 kBq) are shown in Figure 7 (data points, [4]). The CCD97 was operated in inverted mode at -20±5°C (to suppress dark current) at a readout rate of 1 MHz (0.3 seconds per frame), with approximately 10^5 frames analysed for Am^{241} and 1.7×10^4 frames analysed for Co^{57} (a large number of frames was required due to the low activity of the source). A higher frame rate and a source with a

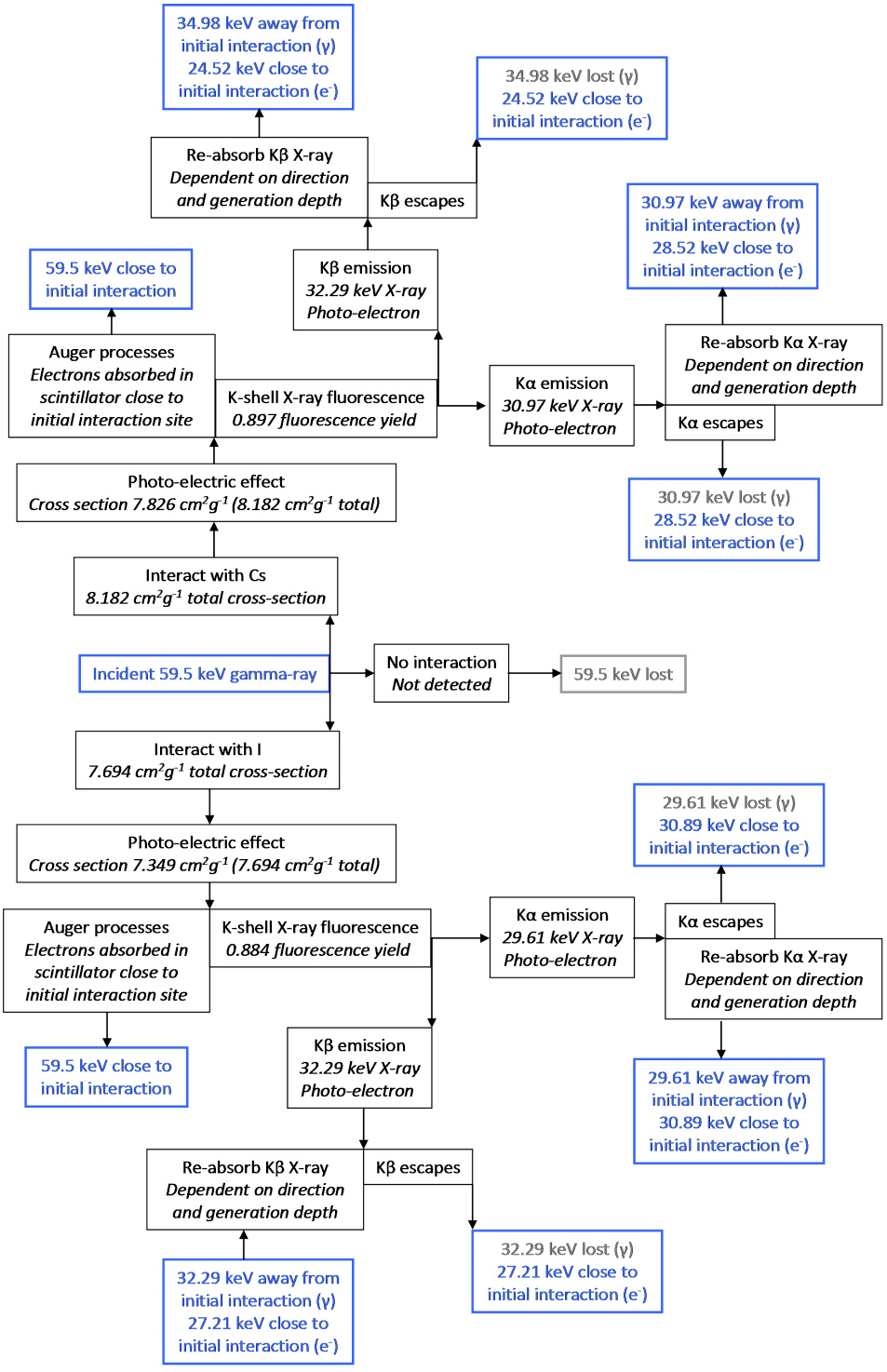

Fig. 6. Flowchart of the interactions incorporated into the simulation process for irradiation of CsI by 59.5 keV gamma-rays.

higher activity could be easily implemented into the system with appropriate electronics and source availability; the increased readout noise from the increased readout speed can be counteracted by an increase in the gain applied with the EM-CCD to remain at an effective readout noise of 1 electron rms. The total number of interactions recorded per frame is the only limit on the activity at any readout speed, such that events must not overlap (no pileup) for the centroiding of individual events to be possible.

The spectrum achieved using Am^{241} shows how the peak at approximately 30 keV dominates over the full-energy peak at 59.5 keV. The peak at approximately 30 keV is formed from many components, namely the re-absorbed fluorescence (Kα and Kβ from both Cs and I), the related escape peaks and fluorescence from the silver foil in the ^{241}Am source. With the limits on the spectral resolution incurred from the intrinsic scintillator resolution and the multiplication gain noise, one cannot separate out the re-absorbed fluorescence events (located away from the primary photon interaction position) from the escape events (at the primary photon interaction position). It is only possible, therefore, to exclude 'all events' around 30 keV in order to remove the re-absorbed fluorescence and therefore to reduce the overall number of counts dramatically by removing the escape events. In this respect, it is therefore essential to determine the requirements of the imaging system and consider a spatial resolution versus count rate trade-off. In the case of the Am^{241} spectrum, there is an element of separation between the peaks at 30 keV and the full-energy peak and therefore one can improve the resolution in the case where this is the priority over the number of counts measured (see Section 11).

The simulated results shown in Figure 7 take the simulation of events discussed in Section 9 and incorporate the energy resolutions shown in Figure 5, measured from the experimental results; each event generated in the simulation has a "recorded energy" randomly generated across a Gaussian profile. The simulations include full-energy events, Kα and Kβ fluorescence from the caesium and iodine in the scintillator, the related escape events and Kα fluorescence from silver (in the ^{241}Am case) and tungsten (in the ^{57}Co case), with the quantity of external fluorescence (silver or tungsten as appropriate) set as a free parameter to be fitted with the experimental data due to the complex geometries and uncertainties involved in quantising the number of fluorescent X-rays generated and subsequently detected.

Taking the case of the ^{241}Am spectrum, Figure 7(a), the appropriate structure can be clearly seen in the simulated results as normalised to the intensity of the 60 keV peak. However, the simulated peak at approximately 30 keV is seen to be higher than that in the experimental results, with a dip in the simulated results at approximately 30-50 keV. This discrepancy between the simulated and experimental results is thought to be due to the methods used to calculate the energy of each event in the experimental case. The overestimation in the

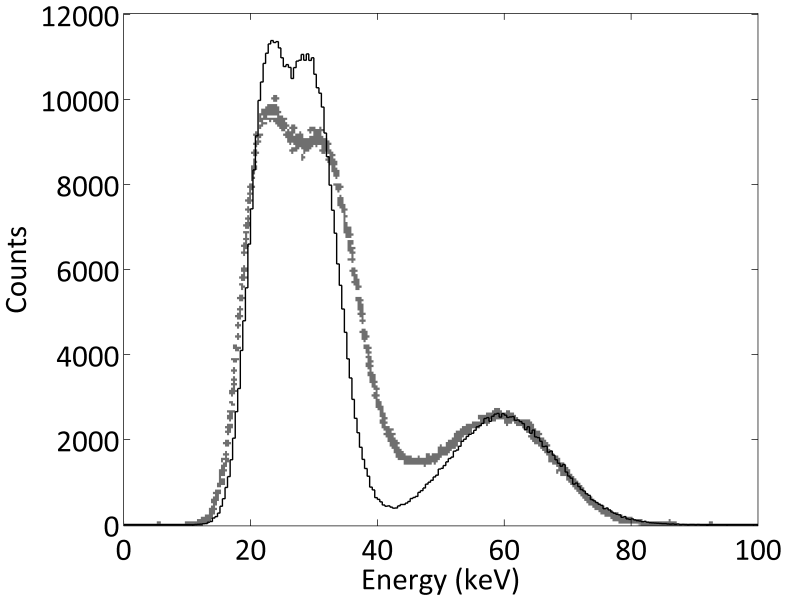

(a) Experimental spectra for Am^{241} (data points) and the simulated spectrum (solid line).

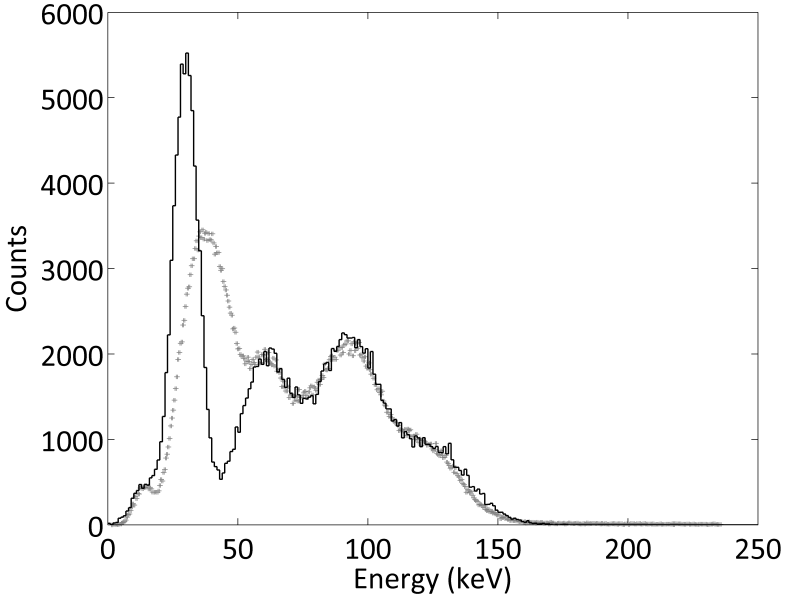

(b) Experimental spectra for Co^{57} (data points) and the simulated spectrum (solid line).

Fig. 7. (a) The spectrum achieved experimentally from the Am^{241} source (data points, [4]) shows the components at the energies specified in the flowchart from Figure 6. A cut-off at approximately 40-50 keV allows the removal of some of the reabsorbed fluorescence, but this removes the bulk of the escape events also and therefore dramatically reduces the number of counts. (b) The experimental spectrum obtained using Co^{57} (data points, [4]) can be explained following a similar analysis as shown in Figure 6 but for Co^{57}. The peak at approximately 60 keV is thought to be the detection of Kα fluorescence from the tungsten edge.

peak at approximately 30 keV is approximately equal to underestimation of the spectrum around 40 keV. Although the simulation accounts for directly coincident events, interactions in close proximity that are not counted as single events lead to an increased energy being attributed to some events, Figure 8. It is thought that the dip in the simulated spectrum can be accounted for in this way.

In order to demonstrate the further complications that occur when using a higher energy gamma source, the 122 keV photons from a Co^{57} were imaged and a similar spectrum produced, Figure 7(b). A similar analysis to that detailed in the flowchart in Figure 6 can be used to determine the multiple energies that will be detected from the 122 keV source, including fluorescence from the tungsten edge at approximately 60 keV and the related escape peaks (noting the spectrum achieved from the incident 59.5 keV photons from the previous testing with the Am^{241} source). In decreasing energy, the full-energy peak can be seen at 122 keV, but this is not fully resolvable from the escape peak at approximately 90 keV. The fluorescence of the tungsten edge can be seen at approximately 60 keV. The large peak at approximately 30 keV is formed from several components, namely the reabsorbed fluorescence from the 122 keV incident X-rays and the reabsorbed fluorescence (and corresponding escape peaks) from the tungsten fluorescence. The low energy peak at 14 keV is due to emission from the Co^{57} source at this energy (although much of this has been removed through thresholding). Taking these energies, it is possible to separate the spectrum into the related components, Figure 7(b). In this case, the spatial coincidence of fluorescence, escape and primary events is greatly complicated by the inclusion of the fluorescence from the tungsten edge and the corresponding K-shell fluorescence of the scintillator.

The simulation has again been run for the case of the ^{57}Co and the results shown in Figure 7(b). As detailed for the ^{241}Am case, the intensity of the lower energy peak is overestimated in the simulation, followed by a similar dip around 40 keV. This is thought to be for the same reasons as detailed in the ^{241}Am case, as outlined in Figure 8.

In the case of higher energy sources, therefore, the improvement of the spatial resolution through the removal of fluorescence events must be considered as somewhat more complex. Through the removal of low energy events (for example, below 50 keV), one can remove the re-absorbed fluorescence and leave a higher number of full-energy and escape events than in the Am^{241} case detailed above. However, the detection of many escape events (due to the potential increased overlap between primary energy peak and escape peak) can leave a minor degradation of the spatial resolution from the range of the electrons emitted of a few micrometers for each interaction.

The energy resolution measured for the main peak at 60 keV from the Am^{241}

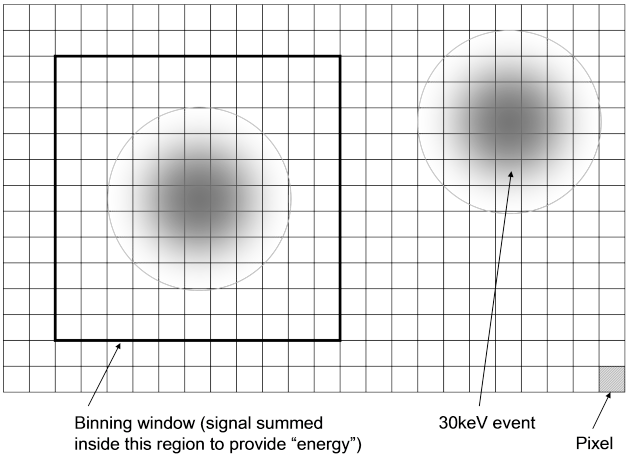

(a) Well separated events.

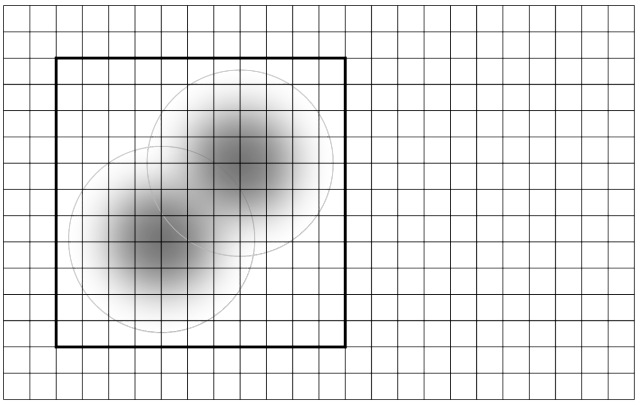

(b) Coincident events.

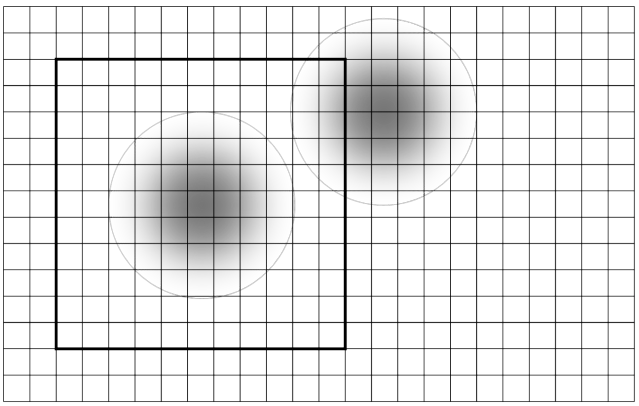

(c) Semi-coincident events.

Fig. 8. The “energy” of each event is assumed to be proportional to the summed signal over a fixed area window surrounding the peak in intensity of each event. (a) Two events have occurred across the pixilated structure of the CCD such that no signal from the second event is summed with the first. The “energy” recorded is that of the first event only. (b) Two events occur in very close proximity, such that the spread of signal from each event creates one “single” event that is recorded with the summed energy (60 keV here). (c) Two events occur a short distance apart such that a fraction of the signal from the second event is included in the “energy” recorded for the first event. The amount of “extra energy” included with the first event will vary with the distance between the events and therefore some of the low energy events will be moved to higher energies in the spectrum across a continuum from 30 keV up to 60 keV, from (a) to (b).

source in the experimental results shown is 33% (20 keV at 60 keV), converging on the limits imposed by the multiplication gain process and intrinsic energy resolution of the scintillator as demonstrated in Figure 5. This result, whilst not reaching the energy resolutions found in the literature for PMT-based gamma cameras (Section 3), the results are consistent with those reported for EM-CCD based camera systems (Section 6). The energy resolution could be improved through the more efficient coupling of the scintillator to the EM-CCD or through the use of a scintillator with a higher light output.

9.2 Positional accuracy

A second simulation has been used to look at the errors involved in the centroiding process when using a 'high spatial-resolution' gamma-camera. Centroiding must be used to provide sub-pixel locations for the event profiles. The sub-pixel locations can be used to create an image that no longer includes the spread of light in the scintillator (as would be found in an integrated image). It is this removal of the light spread that provides the dramatic improvements in spatial resolution detailed in Section 8.2. The noise on the signal does, however, affect the centroiding process. The noise components of most importance here are the noise on the signal input to the EM-CCD, the noise on the gain process and the readout noise of the device.

The simulation produced for this study creates a Gaussian profile with parameters based on the experimental data of [2]. The central point of the Gaussian profile (FWHM of 38 µm and peak signal of 80 electrons at 60 keV, scaling linearly with energy) is positioned in the two extremes of the pixel location: in the centre and in the corner of the pixels. Edge effects are apparent in the centroiding process of this noiseless signal due to the use of the 'centre of mass' approach, as one would expect, where the calculated centroid positions are biased towards the centre of the pixel. These effects can be corrected for using the η-algorithm [41]. One is then able to simulate the noise on the signal and add readout noise (in this case 10 electrons rms) to simulate the noise sources for an 'equivalent non-EM CCD' running at approximately 1-2 MHz (effectively the CCD97 with multiplication gain of one to allow direct comparison with the same pixel sizes). A second option is to apply gain and subsequently add the noise component from the gain process and the readout noise to simulate the noise sources for an EM-CCD. The results from these tests with varying energy are shown in Figure 9, demonstrating the 'best case' centroiding performance if no other degrading factors relating to the scintillator are considered.

The centroid error, as shown in Figure 9, refers to the difference between the input Gaussian central location and that calculated from the centroid

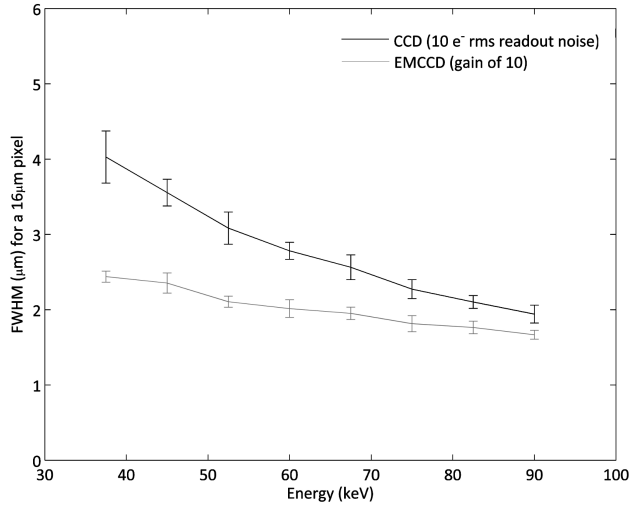

(a) Centre of the pixel.

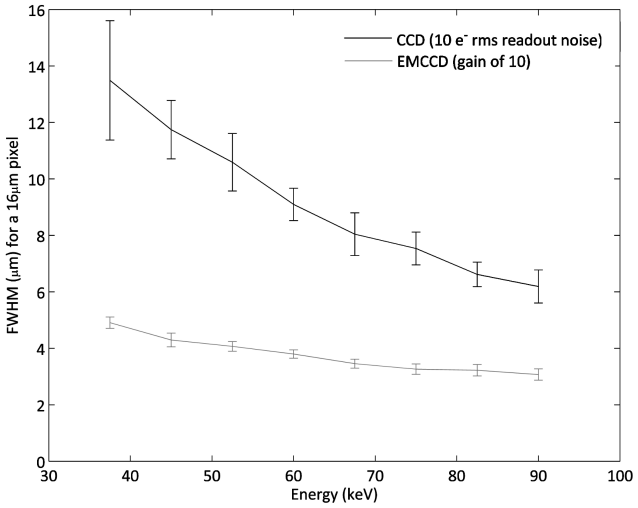

(b) Corner of the pixel.

Fig. 9. A comparison of the expected optimal centroiding accuracy using a simple 3×3 "centre of mass" for a standard non-EM CCD as discussed previously (10 electrons rms readout noise) and an EM-CCD (with a gain of 10) from simulations of a representative Gaussian profile (FWHM of 38 μm and peak signal of 80 electrons at 60 keV, scaling linearly with energy) placed in the centre (a) and corner (b) of a pixel. The excess noise from the gain process, when coupled with the reduction in the effective readout noise, has minimal impact and the 'best case' resolution improves beyond that of the standard CCD. The effects are emphasised for the corner of the pixel where the signal does not 'peak' in one pixel, but instead is shared over four pixels in a 2 × 2 grid, with subsequent reductions in signal for the the neighbouring pixels, as defined by a Gaussian profile placed in the corner of the pixel.

algorithm ("centre of mass" on a 3 × 3 pixel area around the pixel of peak signal) following the inclusion of the specified noise sources. Centroiding errors are provided across a range of energies relevant to this study where a 60 keV event is said to peak at approximately 80 photons for events in which the signal is centred around the centre of a pixel.

It is clear from Figure 9 that the EM-CCD offers improved performance over the equivalent CCD in all cases, shown here for a Gaussian with FWHM of 38 µm on a pixel size of 16 µm for both the CCD and EM-CCD. The effects are more pronounced at lower energies as the signal-to-noise ratio is reduced in comparison to the higher energy cases. When the event signal is centred over the corner of a pixel, the peak signal, to a first approximation, may be considered as almost one quarter of that in the pixel-centre case, hence producing a large reduction in the signal-to-noise ratio and therefore offering very poor spatial centroiding performance when using a standard CCD. The EM-CCD, however, performs consistently well over all energies and event locations in the pixel.

The simulated optimal centroiding accuracy data discussed above show that the noise on the gain process has little effect on the accuracy of the centroiding process, despite the added problems caused to the spectral resolution discussed in Section 8.3. If operating at the high-readout speeds required for many photon-counting applications, the readout noise of the standard CCD could be expected to be higher than the 10 electrons rms used in the simulations here and hence the low-noise performance of the EM-CCD becomes essential to maintain the centroiding accuracy.

10 The impact of internal X-ray fluorescence on spatial resolution

Previous experimental studies have detailed the observation of reabsorbed fluorescence events detected outside the area of imaging area [2,4,13,14]. Our simulations are consistent with hypothesis that the two Gaussians seen in the LSF, as demonstrated in Figure 4(a), result from the initial interaction events (sharper profile) and the re-absorbed fluorescence events (broader profile). The impact of the broader profile is dramatic and can be seen in the MTF curves shown in Figure 4(b) as the sharp drop in MTF at low spatial frequencies. If one was to use lower energy X-rays (with energies below the ionisation energy of the components of the scintillator) one would expect the MTF to be greatly improved, following the form of the MTF shown here at higher frequencies, but now across all frequencies.

10.1 Simulating the impact of re-absorbed fluorescence on the edge spread function

In order to separate out the impact of re-absorbed fluorescence on the spatial resolution of a gamma camera, all aspects of the detector itself must be removed. To this end, a simulation of a camera system with a perfect Edge Spread Function (ESF), a step-function from zero to one, was produced to match the detector used in the previously mentioned experimental programme [2]. The detector is formed from a 1 cm square CsI scintillator of thickness 70 µm. For the purposes of this simulation, all 'detector' aspects of the resolution are to be removed, hence the interactions of photons in the scintillator are assumed to be point-like and depth of interaction effects and light spread are not included in the resulting ESF. In this way, one can separate out the purely fluorescence-induced effects. It is therefore possible to simulate the equivalent set-up to that used experimentally to determine the ESF and LSF, but here with the 'detector' components removed.

The experimental set-up has been simulated through the provision of incident photons of 60 keV to the simulation across a set area only (to simulate an effective tungsten edge). The interactions in the scintillator are tracked and the location of photon interactions in the scintillator are recorded. The results produced show a clear curvature of the ESF. For the 'perfect detector' as simulated here, one would expect a sharp step-function, however, the ESF is anything but sharply defined. The curvature is consistent with that seen experimentally and shows clearly the influence that the re-absorbed internal fluorescence has on the edge of an object being imaged, Figure 10. The recognisable curvature to the ESF is seen in the simulated results in which only the re-absorbed fluorescence is included; no other aspects that might degrade the detector resolution have been included. This curvature to the 'perfect' detector response is responsible for the secondary, broader Gaussian component of the LSF seen in the experimental results of Figure 4(a) and can be seen to stretch across several hundred micrometers as implied in Figure 3 in which the distribution of re-absorbed fluorescence in the xy plane is displayed. This therefore demonstrates that the secondary Gaussian in the LSF can be caused by the re-absorption of the fluorescence X-rays. In the experimental data, the 'curvature' displayed here is convoluted with the detector response (the central, more narrow, Gaussian shown in the experimental LSF, Figure 4(a)).

10.2 Re-absorption distance and the energy resolution

Referring back to Figure 3, one can see that for this example of using a 70 µm thick CsI(Tl) layer with an incident photon energy of 60 keV, the initial event

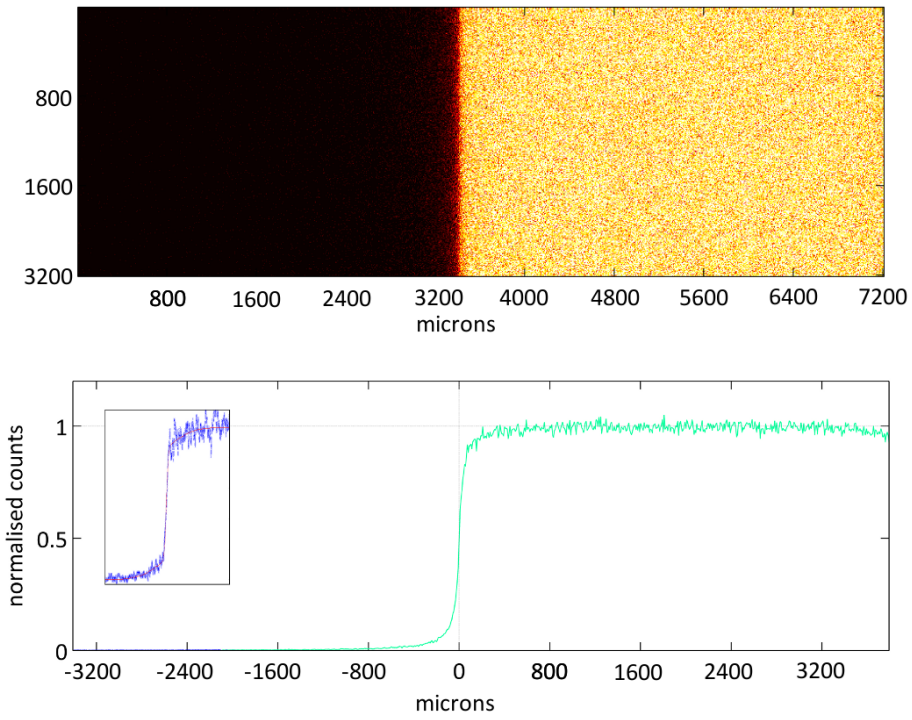

Fig. 10. Top: A simulated image of an edge for a detector system with a perfect (step-function) ESF if internal fluorescence were to be ignored. Recorded events are not limited to the right hand half of the image upon which the photons were incident to the system, showing the influence of the re-absorbed internal X-ray fluorescence (in this case for 60 keV incident photons in a 70 µm thick CsI:Tl layer). Bottom: Without re-absorbed fluorescence one would expect a perfect step-function, with the roll-over of the signal demonstrating the presence of signal from the re-absorbed fluoresence, as displayed in the inset ESF from experimental data.

and the re-absorbed fluorescence X-ray will be included in the same 'event' if the detector spatial resolution is of the order of a few hundred micrometres or more. Not only is this the case, but if a much larger pixel size is used with individual scintillator modules, one can also capture additional visible photons from reflections occurring at the edges of the scintillation objects and it then becomes possible to achieve energy resolutions of the order of the limits of the scintillation process itself. With this greatly improved energy resolution, however, comes a significant reduction in the spatial capabilities of the device as the effective binning of the signal increases the size of each imaging 'pixel'.

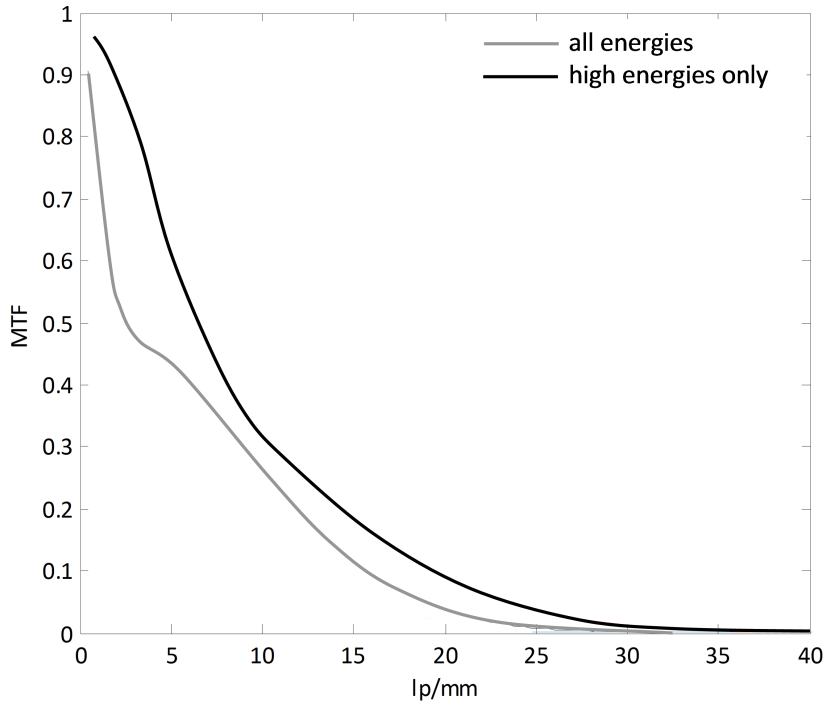

Fig. 11. Results from the same experimental campaign as detailed in Section 8. An energy threshold of 45 keV was used to remove many'low energy' events and hence remove a portion of the fluorescent and escape events. The improved resolution is shown by the improved MTF across all spatial frequencies, but particularly at high spatial frequencies (a factor of 2 improvement at 20 lp/mm).

11 Reducing the impact of the internal X-ray fluorescence

It has been detailed in [2] that through the use of energy discrimination (using the calculated energy of a profile through methods as described in Section 8.3) one can remove the many of the re-absorbed fluorescence events. This process does, however, come at a cost to the effective detection efficiency, as a large number of primary interaction events will also be removed, leaving only approximately 10% of events for which no X-ray fluorescence occurs when imaging at 60 keV. At 60 keV, for a ^{241}Am source, the spatial resolution (FWHM of the LSF) can be improved from 31 µm to 25 µm [2], although this improvement in FWHM is mostly due to the removal of the escape electrons which are responsible for 'events' recorded a few micrometers away from the initial interaction positions. The main improvement from the energy discrimination process is instead that of the reduction in the intensity of the broader Gaussian component of the LSF, that due to the fluorescence, and hence a much improved MTF and greatly improved imaging performance, Figure 11.

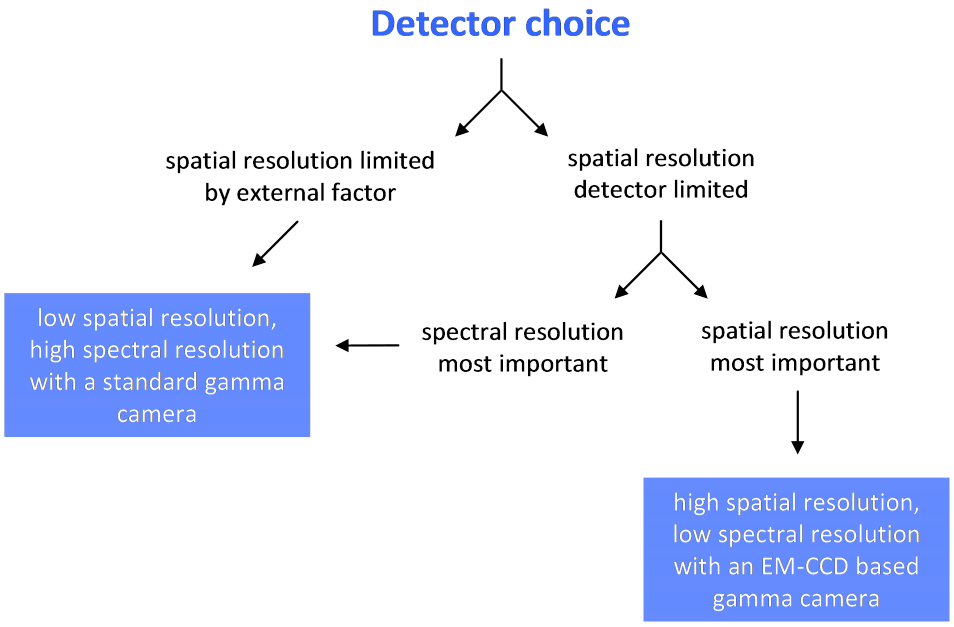

Fig. 12. Simplified summary of the most appropriate gamma camera detector choice.

12 Related detector developments

Over recent years, the development of hybrid pixel detectors has brought the possibility of high spatial resolution detectors which are capable of also providing a high energy resolution. The bonding of CdTe and CdZnTe detectors to CMOS readout chips has enabled a combined performance to be achieved, albeit on the small area scale as one loses the option to apply optics to expand the imaging area (such as a lens system or through fibre-optic tapering). Results reported so far include an intrinsic spatial resolution of 75 µm at 122 keV in studies detailed in [20] using a CdTe pixel detector ($14\times14\times1$ mm^2) with 256×256 square pixels and a 55 µm pitch. This pixel detector is coupled to a CMOS single photon counting integrated circuit from the Medipix2 series. In similar early developments using a CdZnTe sensor, a FWHM (at room temperature) at 122 keV of 2.5% has been reported [42], although no spatial results are presented.

13 Conclusions

The choice of detector for X-ray imaging, as with all applications, must be carefully considered, as the experimental and simulated data presented here have shown. The most appropriate choice of detector can be briefly summarised as shown in Figure 12.

If the spatial resolution of a system is limited by an external factor such as the collimators used in medical imaging, then the scintillator-coupled EM-CCD is the optimal detector choice. The dramatic improvement in spatial resolution over more traditional X-ray imaging systems has negligible impact on the images taken due to the limits on the resolution set by the collimator. A lower spatial resolution system, one with a better energy resolution, should be the imaging system of choice. The spectral performance of gamma-cameras based on the PMT (Section 3) cannot be reached by current EM-CCD based systems in which the limit with CsI(Tl) has been shown to be approximately 20-30% using americium-241 with a 1:1 fibre-optic plate. Using scintillators with a higher light output would improve the spectral resolution but the increase in noise from the multiplication gain process cannot yet be overcome.

If one is not limited spatially by external sources, then the scintillator-coupled EM-CCD should be seriously considered. Imaging for synchrotron-based applications where high resolution, high sensitivity and a high signal-to-noise ratio are required may benefit greatly from the improved spatial resolution when low fluxes are required to be measured to a high positional accuracy, although care would be required in appropriately shielding the detector from direct detection to prevent damage to the EM-CCD and the electronics. For example, in macromolecular crystallography, the high spatial resolution will bring the ability to better resolve closely lying distributions of peaks whilst improving the signal-to-noise ratio for low intensity peaks. In systems in which the integration imaging mode is predominantly used, the improvements through photon-counting with such a detector allow the basic use of energy discrimination that would not otherwise be possible. However, the energy resolution of a high-resolution gamma-camera such as this is limited by the processes through which the high spatial resolution is achieved. By using only a small proportion of the visible photons emitted by the scintillator for each event (to keep the spatial information in the form of the Gaussian-like event profile), the noise on the detected signal is comparatively high and is increased further still through the gain process of the EM-CCD (required to keep the effective readout noise low at the high frame-rates required for photon-counting imaging).

In systems in which the energy of the incident X-rays is lower than the K binding energy of the scintillator elements (less than approximately 30 keV for CsI), the problems associated with internal ionisation are no longer present and the scintillator-coupled EM-CCD is expected to provide further improvements in spatial resolution and MTF.

Acknowledgements

With thanks to David Burt, Peter Pool and Bill Bruns of e2v technologies. Also with thanks to all members of the e2v Centre for Electronic Imaging, past and present, who have offered advice and help in the development of this project.

References

[1] Wernick, M. N. and Aarsvold, J. N., "Emission tomography: the fundamentals of PET and SPECT", Academic Press (2004).

[2] Hall, D. J. and Holland, A., "Photon-counting imaging camera for high-resolution X-ray and gamma-ray applications", JINST 6, (2011), C01022.

[3] Hall, D. J., Holland, A. and Smith, D.R., "Imaging and spectroscopy using a scintillator-coupled EMCCD", SPIE 7021, (2008), 70211Z.

[4] Hall, D. J. and Holland, A., "High resolution X-ray and -ray imaging using a scintillator-coupled Electron-Multiplying CCD", Proc. SPIE 7449, (2009), 74491G.

[5] Hall, D. J., Holland, A. and Smith, D. R., "The use of automatic scale selection to improve the spatial and spectral resolution of a scintillator-coupled EMCCD", Nucl. Instr. Meth. A 604, (2009) 207-210.

[6] Hall, D. J. (2010) "Exploring the impact of detection physics in X-ray CCD imagers and spectrometers". PhD thesis. The Open University.

[7] Elster, J. and Geitel, H. F., "About the scintillating phosphorence of the Sitoblende excited by radioactive emanations", Physikalische Zeitschrift 4, (1903), 439.

[8] Rodnyi, P., "Physical processes in inorganic scintillators", first edition, CRC Press, Florida, 1997, ISBN: 0-8493-3788-7.

[9] Schotanus P., Kamermas R., and Dorenbos P., "Scintillation characteristics of pure and Tl-doped CsI crystals", IEEE Trans. Nucl. Sci., 37(2) (1990) 177182.

[10] Bass M., DeCusatis C., Li G., Mahajan V. N., Enoch J., Van Stryland E., Optical Society of America, "Handbook of Optics", third edition, Vol. 4. McGraw-Hill, 2009, ISBN: 0-0714-9892-3.

[11] Bill Bruns, e2v, private communication.

[12] Krause M. O., "Atomic Radiative and Radiationless Yields for K and L Shells", J. Phys. Chem. Ref. Data 8, 307 (1979)

[13] Nagarkar, V.V., Shestakova, I., Gaysinskiy, V., *et al.*, "Fast X-ray/γ-ray imaging using electron multiplying CCD-based detector", Nuclear Instruments and Methods in Physics Research Section A 563(1) (2006) 45-48.

[14] Miller, B. W., Barber, H. B., Barrett, H. H., Shestakova, I., Singh, B., and Nagarkar, V. V., "Single-photon spatial and energy resolution of a columnar CsI(Tl)/EMCCD gamma-camera using maximum-likelihood estimation", SPIE 6142, (2006), 61421T.

[15] Pani, R., Pellegrini, R., Cinti, M., N., *et al.*, "Recent advances and future perspectives of position sensitive PMT", Nucl. Instr. Meth. A, 213 (2004) 197-205.

[16] Pani, R., Pellegrini, R., Cinti, M., N., *et al.*, "A novel compact gamma camera based on flat panel PMT", Nucl. Instr. Meth. A, 513 (2003) 36-41.

[17] Xi,. W., Seidel, J., Kakareka, J., *et al.*, "MONICA: a compact, portable dual gamma camera system for mouse whole-body imaging", Nucl. Med. Bio. 37 (2010) 245-253.

[18] Yamamoto, S., "Resolution Improvement Using a Fiber Optic Plate for a Small Field-of-View NaI(Tl) Gamma Camera", IEEE Trans. Nucl. Sci., 53(1) (2006) 49.

[19] Yamamoto, S., Imaizumi, M., Shimosegawa, E., and Hatazawa, J., "Development of a compact and high spatial resolution gamma camera system using $LaBr_3$(Ce)", Nucl. Instr. Meth. A, 622 (2010) 261-269.

[20] Russo, P., Mettvier, G., Pani, R., Pellegrini, R., Cinti, M., N., and Bennati., P., "Imaging performance comparison between a $LaBr_3$:Ce scintillator based and a CdTe semiconductor based photon counting compact gamma camera", Med. Phys. 36 (2009) 1298.

[21] Janesick, J., "Scientific Charge-Coupled Devices", first edition, *SPIE Press*, Washington, 2001, ISBN: 0-8194-3698-4.

[22] Miller, B. W., Barber, H. B., Barrett, H. H., Wilson, D. W., and Liying C., "A Low-Cost Approach to High-Resolution, Single-Photon Imaging Using Columnar Scintillators and Image Intensifiers", IEEE Nuclear Science Symposium Conference Record 6, (2006), 3540-3545.

[23] Miller, B., W., Barber, H., B., Barrett, H., H., Chen, L. and Taylor, S., J., "Photon-counting gamma camera based on columnar CsI(Tl) optically coupled to a back-illuminated CCD", SPIE 6510, (2007), 65100N.

[24] Jerram, P., Pool, P., Bell, R., Burt, D., Bowring, S., Spencer, S., Hazelwood, M., Moody, I., Catlett, N., and Heyes, P., "The LLLCCD: Low light imaging without the need for an intensifier", Proc. SPIE 4306 (2001) 178-186.

[25] Mackay, C., D., Tubbs, R., N., Bell, R., Burt, D., Jerram, P., and Moody, I., "Sub-electron read noise at MHz pixel rates", Proc. SPIE 4306, (2001), 289-98.

[26] Jerram P. A., Pool P. J. , Burt D. J., Bell R. T., Robbins M. S., "Electron Multiplying CCDs", SNIC Symposium (Stanford, California), 3-6 April 2006.

[27] Burkhardt M., and Schwille P., "Electron multiplying CCD based detection for spatially resolved fluorescence correlation spectroscopy", Optics Express, 14(12) (2006) 5013-5020.

[28] Lees J. E., Bassford D. J., Blake O. E., Blackshaw P. E. and Perkins A. C., "A high resolution Small Field Of View (SFOV) gamma camera: a columnar scintillator coated CCD imager for medical applications", JINST 6 (2011) C12033

[29] Robbins, M., S. and Hadwen, B., J., "The Noise Performance of Electron Multiplying Charge-Coupled Devices", IEEE Transactions On Electron Devices 50(5), (2003), 1227-1232.

[30] J. H. Tutt, D. J. Hall, R. D. Harriss, A. D. Holland, and N. J. Murray, "The Noise Performance of Electron Multiplying Charge-Coupled Devices at X-rays energies", IEEE trans. Elec. Devices, In Press.

[31] de Vree, G., A., van der Have, F. and Beekman, F., J., "EMCCD-based photon-counting mini gamma camera with a spatial resolution $<$ 100 µm", IEEE Nuclear Science Symposium Conference Record 5 (2004) 2724-2728.

[32] Vree, G. A. d., A. H.Westra, *et al.*, "Photon-Counting Gamma Camera Based on an Electron-Multiplying CCD", IEEE Trans. Nucl. Sci. 52(3) (2005) 580-588.

[33] Beekman, F., J., and de Vree, G., A., "Photon-counting versus an integrating CCD-based gamma camera: important consequences for spatial resolution", Phys. Med. Biol. 50 (2005) N109-N119.

[34] Heemskerk, J., W., T., Westra, A., H., Linotte, P., M., Ligtvoet, K., M., Zbijewski, W. and Beekman, F., J., "Frontilluminated versus back-illuminated photon-counting CCD-based gamma camera: important consequences for spatial resolution and energy resolution", Phys. Med. Biol. 52 (2007) N149-N162.

[35] Lindeberg, T., "Scale-Space Theory in Computer Vision", Kluwer Academic Publishers (1994).

[36] Korevaar, M., A., N., Heemskerk, J., W., T., Goorden, M., C., and Beekman, F., J., "Multi-scale algorithm for improved scintillation detection in a CCD-based gamma camera", Phys. Med. Biol. 54 (2009) 831-842.

[37] R. Pani, M.N. Cinti, R. Pellegrini, P. Bennati, M. Betti, F. Vittorini, M. Mattioli, G. Trotta, V. Orsolini Cencelli, R. Scafe, F. Navarria, D. Bollini, G. Baldazzi, G. Moschini, F. de Notaristefani, "$LaBr_3$:Ce scintillation gamma camera prototype for X and gamma ray imaging", Nuclear Instruments and Methods in Physics Research A 576 (2007) 1518.

[38] e2v CCD97 data-sheet, A1A-CCD97BI_2P_IMO Issue 3 (2004).

[39] Hubbell, J.H. and Seltzer, S.M. (2004), Tables of X-Ray Mass Attenuation Coefficients and Mass Energy-Absorption Coefficients (version 1.4). Available: http://physics.nist.gov/xaamdi (25 January 2011). National Institute of Standards and Technology, Gaithersburg, MD. Originally published as NISTIR 5632, National Institute of Standards and Technology, Gaithersburg, MD (1995).

[40] Shah, K., S., Glodo, J., Klugerman, M., Higgins., W., M., Gupta, T., and Wong, P., "High Energy Resolution Scintillation Spectrometers", IEEE Trans. on Nucl. Sci., 51(5) (2004) 2395-2399.

[41] Turchetta R., "Spatial resolution of silicon microstrip detectors", Nucl. Instr. and Meth. A, 335 (1993) 44-58.

[42] Sia, R., Kleinfelder, S., Nagarkar, V., V., "Solid-state photon-counting hybrid detector array for high-resolution multi-energy X-ray imaging", Nucl. Instr. Meth. A, 652 (2011) 470-473.